



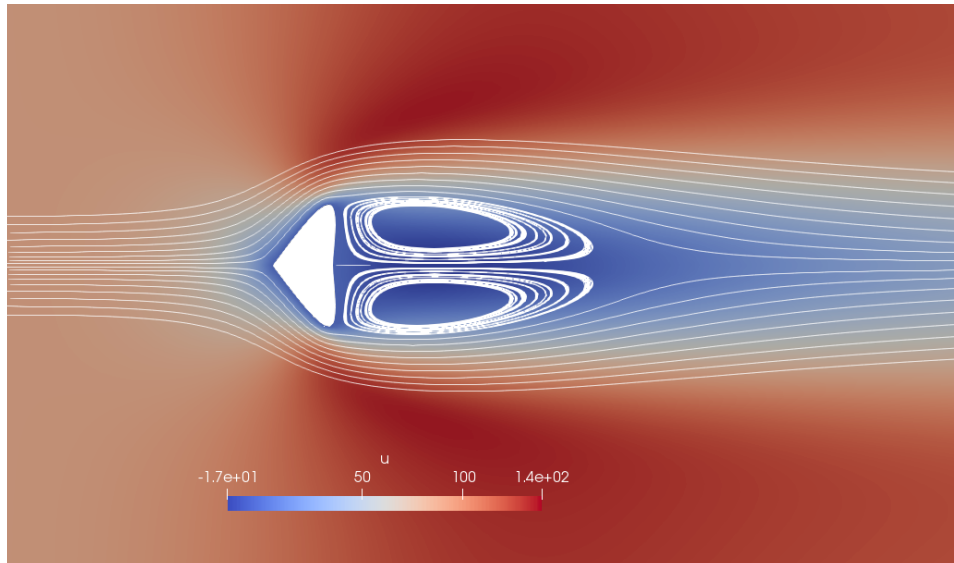
CERFACS
42, Avenue Gaspard Coriolis
31057 Toulouse cedex 01, France

Stanford | ENGINEERING

Stanford University
Mechanical Engineering Department
Flow Physics and Computational Engineering Group

MULTIFIDELITY IN CFD

Collaboration Report



Supervisor at CERFACS:
PhD BÉNÉDICTE CUÉNOT
PhD JEAN-CHRISTOPHE JOUHAUD

Supervisor at Stanford:
Prof. GIANLUCA IACCARINO

Dates of the collaboration:
from April 13th, to May the 4th, 2018

Co-worker at Stanford:
PhD LLUIS JOFRE

Author:
M. PAMPHILE ROY

Contents

1	Introduction	1
2	Multi-fidelity method	1
2.1	Evofusion	1
2.2	Required Design of Experiment	1
2.3	Cost strategy	1
2.4	Quality assessment	1
3	Case description	2
3.1	Geometry	2
3.2	Numerical setup	2
4	Uncertainty Quantification	3
4.1	Parameter space Evaluation	3
4.2	First UQ	3
4.3	Second UQ	3
5	Redesigning the Case	4
6	Bluff body	5
7	Increasing the <i>Reynolds</i>	7
8	Perspectives	7

1 Introduction

The objective of this collaboration is to explore multi-fidelity strategies for high-dimensional Uncertainty Quantification (UQ) in computational flow physics applications. From the literature, there are mainly two approaches: (*i*) *Multi-Level Monte-Carlo* (MLMC); (*ii*) surrogate based analysis. The first one, explored at Stanford, consists in aggregating results on a quantity of interest (QoI) to obtain its mean and variance. The present report focuses on the second approach, used at CERFACS, but the final application will consider a comparison between the two approaches.

2 Multi-fidelity method

2.1 Evofusion

In (Kennedy and O'Hagan 2000), they proposed a methodology to combine several levels of fidelity. The final surrogate's covariance matrix takes into account all fidelity using a Markov assumption. Which is to say that at concordant points, we cannot learn any more information from the data. (Courrier et al. 2016) have made an extensive comparison of different multi-fidelity strategies on both analytical functions and real applications. They concluded that the simplest one was also found to be the most robust one.

Considering two levels of fidelity f_e and f_c , respectively an expensive and a cheap function expressed as a computational cost. The *evofusion* model (Forrester et al. 2006) is expressed as

$$\hat{f}(x) = f_c(x) + \hat{f}_\epsilon(f_e(x), f_c(x)), \quad (1)$$

with \hat{f}_ϵ the surrogate model representing the discrepancy between the two fidelities.

2.2 Required Design of Experiment

A rule of thumb is to sample the parameter space using $n = 10k$ (Forrester et al. 2007), with k the number of dimensions. All technic share the same needs regarding the constructions of the respective DoE. A nested design is required in order to get the impact of the fidelity on the QoI. If using low discrepancy sequences, this is not an issue. By design, these sequences ensure good properties for any number of points. Thus, one can compute a design for the low-fidelity model and use the beginning of the sequence to set the high fidelity design. The problem arises if using random sequences. In this case, there is no direct link to make and it becomes a combinatory problem (Forrester et al. 2007).

2.3 Cost strategy

A cost ratio α between the two can be defined as:

$$\alpha = \frac{f_e}{f_c}. \quad (2)$$

Using this cost relationship and setting a computational budget C , it is possible to get a relation between the number of cheap and expensive realizations.

$$C f_e = N_e f_e + N_c f_c, \quad (3)$$

$$C f_e = N_e f_e + N_c \frac{\alpha}{f_e}, \quad (4)$$

$$C = N_e + N_c \alpha, \quad (5)$$

$$N_c = \frac{C - N_e}{\alpha}. \quad (6)$$

As the design being nested, the number of cheap experiments must be strictly superior to the number of expensive ones. Indeed, the opposite would result in no additional information to the system.

2.4 Quality assessment

The quality of the model is measured using a dataset composed of high fidelity simulations. Based on this

dataset, two metrics are computed, the predictive coefficient Q_2 (Marrel et al. 2009) and the *Kolmogorov-Smirnov* statistical test (Clarke et al. 1992).

The Q_2 reads:

$$Q_2 = 1 - \frac{\sum_{k=1}^{N_{\text{ref}}} \left(f^{(k)} - \hat{f}^{(k)} \right)^2}{\sum_{k=1}^{N_{\text{ref}}} \left(f^{(k)} - \bar{f} \right)^2}. \quad (7)$$

Regarding the *Kolmogorov-Smirnov* statistical test, it compares two empirical cumulative distribution functions (CDF) F and G . The test statistic is:

$$D = \sup_x |F(x) - G(x)|. \quad (8)$$

The Kolmogorov-Smirnov test leads us to reject this hypothesis with a type I error $\alpha \in]0, 1[$ when:

$$D > c(\alpha) \sqrt{\frac{n+m}{nm}}, \quad (9)$$

with $c(\alpha)$ found in the literature (?). In the present study, using $\alpha = 0.05$ and $n = m = N_{\text{ref}}$, the null hypothesis is rejected if $D > 6,082 \cdot 10^{-3}$.

3 Case description

3.1 Geometry

The geometry consists in a rectangular channel with a rib. Due to CPU-hour cost, a non-turbulent 2-dimensional case is considered. The objective is to observe the impact of geometrical changes and of the flow in the recirculation zone behind the rib—see Fig. 1. The channel is set with a width of 10 cm and a height of 6 cm. Flow features are described in Table 1.

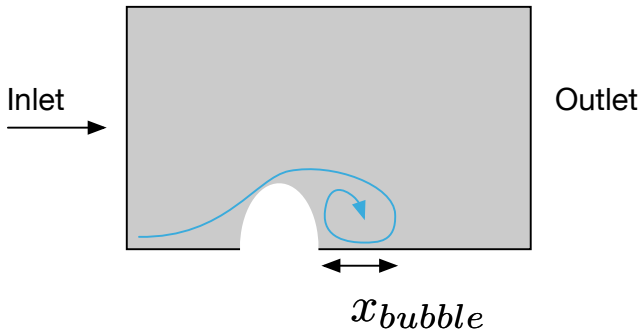


Figure 1: Sketch of the channel configuration

$\mathcal{R}e$	40
P	101 325 Pa
V	85,78 m/s
Convective time	$1,17 \cdot 10^{-3}$ s
Viscosity	0.155

Table 1: Problem parameters

3.2 Numerical setup

AVBP has been used to simulate all cases using best practices—see Table 2. The mesh was created using CENTAUR and is only composed of triangles. Due to the high viscosity and the laminarity of the fluid, the characteristic length of the elements is not limited by the resolution of the boundary layer. It can be set to a high value of $1,2 \cdot 10^{-3}$ which enables to have 40 triangles on the height of the channel. This allows to capture eddies at least of the size of the millimetre. Regarding the low-fidelity case, this characteristic length is divided by two, thus eddies must be at least 2 millimeters to be captured with this resolution. The two meshes are presented in Fig. 2.

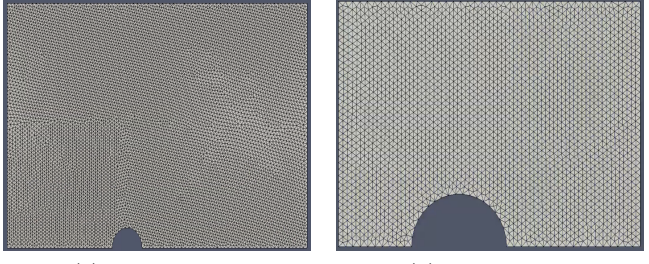


Figure 2: Mesh levels.

In order to validate the nominal case, a refined case with 30 000 nodes was used and no difference was observed. Figure 3 presents the baseline computation. The quantity of interest (QoI), the recirculation bubble's size, is computed with the post-processing library Antares by looking at the shear stress on the wall behind the rib—see Fig. 4.

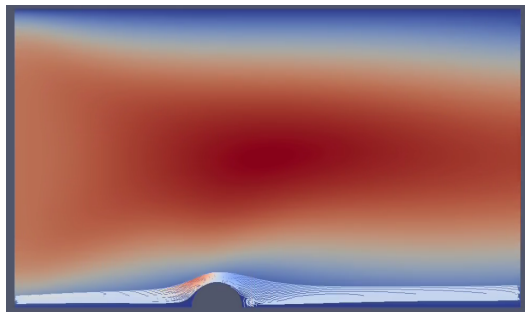


Figure 3: Baseline simulation.

	Low fidelity	High fidelity
Diffusion scheme	FE_2delta	
Convective scheme	TTGC	
LES model	Smagorinsky	
Convective time (ms)	3,5	
Inlet condition	INLET_RELAX_UVW_T_Y	
Outlet condition	OUTLET_RELAX_P	
Wall condition	WALL_NOSLIPADIAB	
Mesh (nodes)	3 600	9 800
y^+	0.39	0.19
CPU time (s)	65	330

Table 2: AVBP numerical setup.

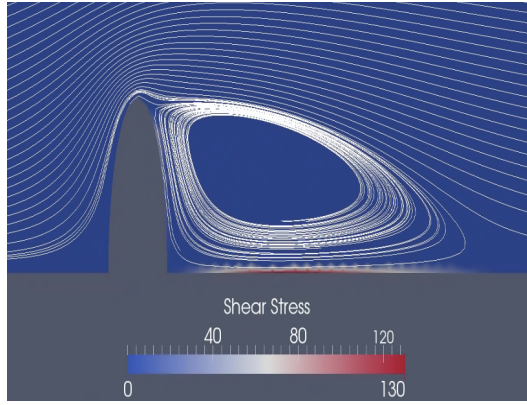


Figure 4: Shear stress on the wall.

4 Uncertainty Quantification

4.1 Parameter space Evaluation

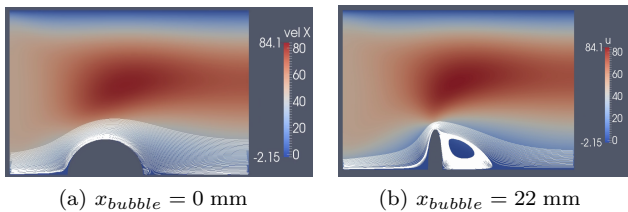


Figure 5: Variation of the size of the recirculation bubble. **a** without recirculation; **b** with a large recirculation.

4.2 First UQ

The first parameter space was composed of 3 random variables—see Table 3—, with two geometrical parameters describing the rib and one feature flow. A total of 90 high fidelity and 220 low fidelity simulations were done. The resulting response surface is shown in Fig. 6. The results are in accordance with our expectations as the

recirculation bubble increase as the shape of the rib tends to a plate. Moreover, the exponent of the inlet velocity profile appears to have no impact on the QoI in regards to the other two parameters. *Sobol'* indices shown that the height of the rib contributed to 83 % of the variance of the QoI versus 13 % for the rib width. From this first study, it can be concluded that the exponent can be replaced by another random variable. Also, range of the height of the rib can be narrowed down to [0,0075, 0,02] and for the width it can go to [0,001, 0,0175].

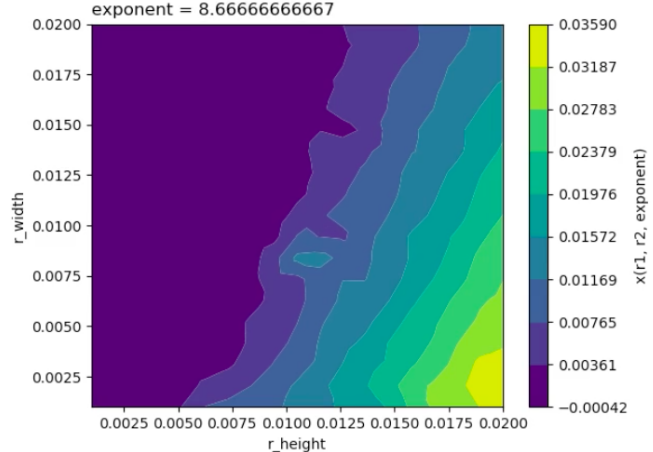


Figure 6: Response surface.

4.3 Second UQ

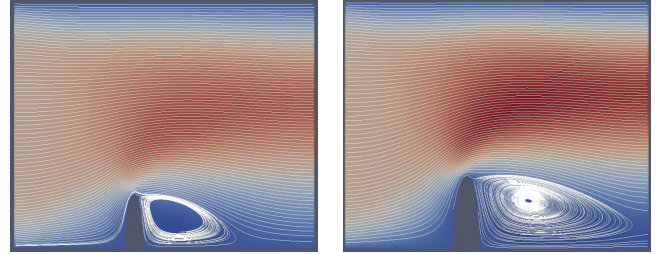
In the second study, bounds have been adapted and the exponent was replaced by the viscosity μ in order to model change in the *Reynolds* number from 40 to 100—see Table 4. Thus low viscosity (respectively high viscosity) accounts for high Reynolds (respectively low Reynolds). At high Reynolds, a bifurcation is observed with high heights and low widths—see Fig. 7. This is explained by a lifting of the recirculation bubble. The bubble is actually not smaller but larger in this case but its lifting impact the shear stress at

Parameter	Variable	Range
2-3 Ellipse width	r_{width}	[0,001, 0,02]
Ellipse height	r_{height}	[0,001, 0,02]
Inlet velocity profile exponent	$exponent$	[2, 10]

Table 3: Parameter space definition.

Parameter	Variable	Range
2-3 Ellipse width	r_{width}	[0,001, 0,0175]
Ellipse height	r_{height}	[0,00075, 0,02]
Viscosity	μ	[0,062, 0,155]

Table 4: Parameter space definition.



(a) Not lifted: $r_{height} = 0.013$, $r_{width} = 0.003$, $\mu = 0.066$ (b) Lifted: $r_{height} = 0.018$, $r_{width} = 0.004$, $\mu = 0.064$

the wall. Figure 8 presents two cases close to each other in the parameter space. Similar points with lower Reynolds did not exhibit any lifting. Thus it is the high Reynolds that is the cause of this phenomenon.

! It appeared that this was due to the domain. When increasing the domain size, the bubble is correctly attached.

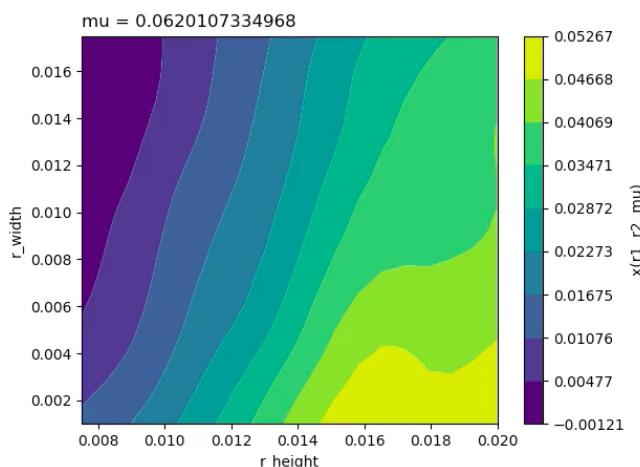


Figure 7: Response surface.

Figure 8: Two configurations at high Reynolds with large recirculation bubble.

Metrics defined in Section 2.4 are computed for a set of numbers of high fidelity N_e with respect to a total cost C —see Fig. 9.

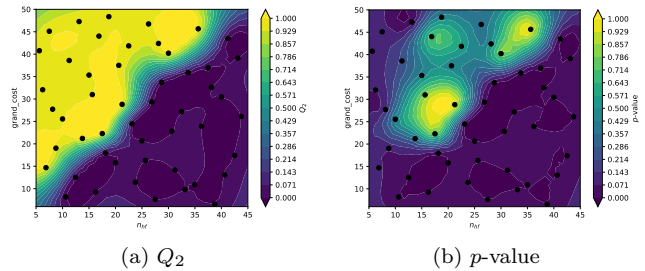


Figure 9: Metrics in terms of the number of high fidelity and total cost in terms of high fidelity.

5 Redesigning the Case

As seen previously, the boundaries were too close to the rib so that the recirculation zone was not correctly predicted. The domain was extended and now the bubble is not lifting at all Fig. 10. Moreover, at low fidelity, the geometry was too much deteriorated. A constrain on the mesh is now used to have the correct shape even at low fidelity. As the velocity at the wall is low, this only slightly impact the CFL constrain.

In the following, dimensions have been normalized using the maximal dimension of the ellipse: $D = 0,02$ mm. The parameter space is adapted in consequence—see Table 5.

Parameter	Variable	Range
2-3 Ellipse width	r_{width}	[0,05, 0,875]
Ellipse height	r_{height}	[0,375, 1,0]
Viscosity	μ	[0,103, 0,258]

Table 5: Parameter space definition.

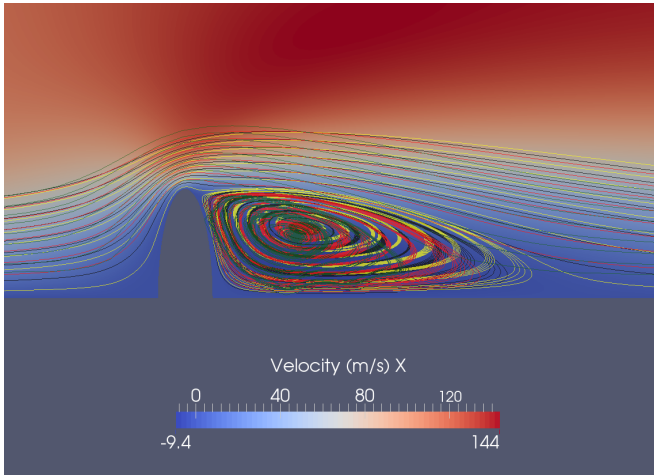


Figure 10: Comparison of the recirculation zone with different meshes.

Apart from the bubble lifting, the results are the same regarding the overall response surface and the sensitivity indices. To complement the study, two velocity profiles have also been considered. There are located just after the rib and at 1D. Total sensitivity indices show the same results as for the size of the recirculation but spacial indices indicate that just on top of the rib, the most important factor is not anymore the height but the Reynolds—see Fig. 11. At 1D, this is not observed and the height is the most important factor all along the profile. This phenomenon can be explain by the development of a shear layer at this location. No further investigation is performed as we decided to move to change the configuration.

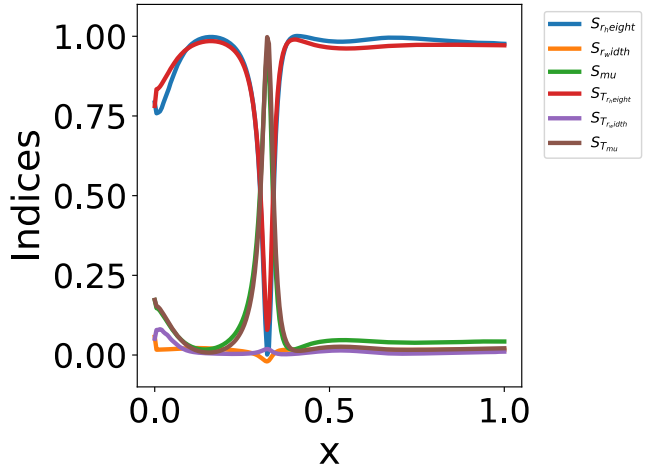


Figure 11: Spatial Sobol' indices of the recirculation size along the profile on y -axis at 1D after the rib.

6 Bluff body

From the previous results, it seems that the top wall is truly constraining the flow, also, the rib is located in the boundary layer due to the bottom wall. So the effect of geometrical modification is constrained by these walls. Thus, a new configuration is done. It consists on top of a wall slip boundary condition and of a symmetry plane at the bottom. Experience from the previous cases is used to constrain the mesh. The domain is further extended in order for the wake to adapt. The domain is 26D long and 10D large. There are 5D before the bluff body, 5D above and 20D after it—see Fig. 12.

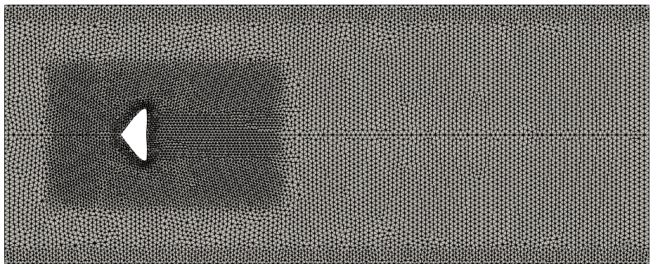


Figure 12: Bluff body domain.

Due to the symmetry plane at the bottom, the QoI cannot be measured using the shears. Thus the sign change in the axial velocity on the centre line is used as shown in Fig. 13. Concerning the definition of the bluff, it has been adapted to have more flexibility in the geometry by using a control point along with leading and trailing point of the bluff being fixed to have a constant width of 1D—see Table 6. Figure 14 shows some example of the parameter space exploration. The position of the control point on the x -axis as only a slight impact compared to

Parameter	Variable	Range
2-3 Point x	p_x	$[-0.49, 0.49]$
Point y	p_y	$[0.1, 1.0]$
Viscosity	μ	$[0.103, 0.258]$

Table 6: Parameter space definition.

the *Reynolds*. This is confirmed with the response surface (see Fig. 15).

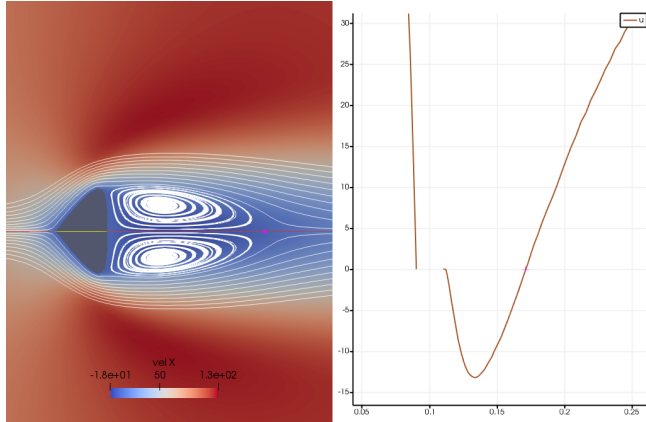


Figure 13: Axial velocity profile on the centre line.

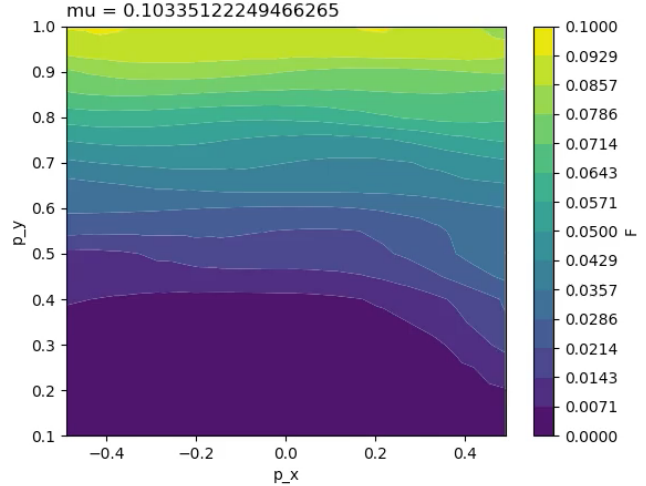
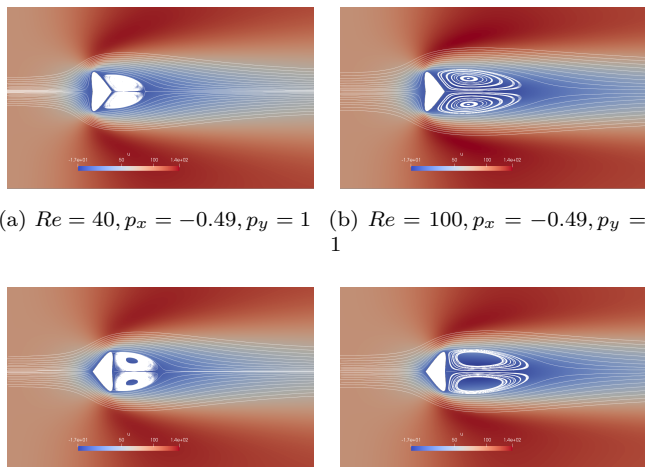


Figure 15: Response surface.

From Fig. 16 and Fig. 17, the position of the control point on the y -axis is again the most influent factor. However, at $y \simeq 0.035$ all parameters have no influence. This region corresponds to a shear region. We suppose that the fact that the parameters have no impact on the location of this region is due to the extreme laminarity of the flow. Due to this observation and to the relative linearity of the response on the QoI, we decided to increase the *Reynolds* to 3900 Kravchenko and Moin (2000); Parnaudeau et al. (2008).



(a) $Re = 40, p_x = -0.49, p_y = 1$ (b) $Re = 100, p_x = -0.49, p_y = 1$

Figure 14: Parameter space exploration.

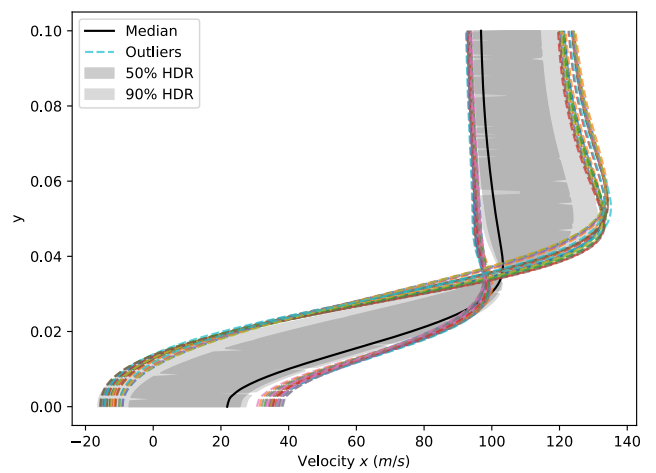


Figure 16: Axial velocity profile on y -axis at $1D$ after the bluff body.

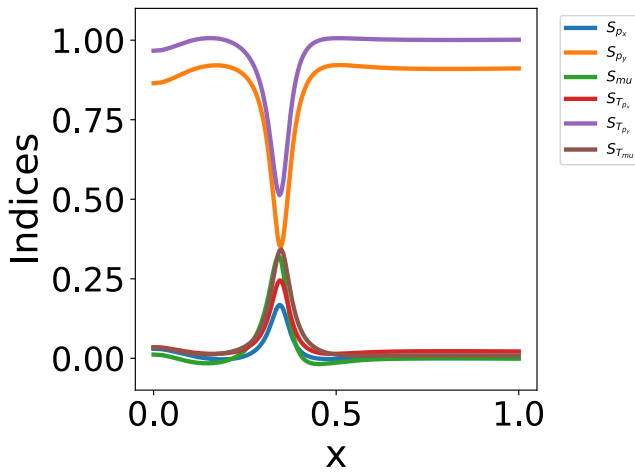


Figure 17: Spatial Sobol' indices of the recirculation size along the profile on y -axis at 1D after the bluff body.

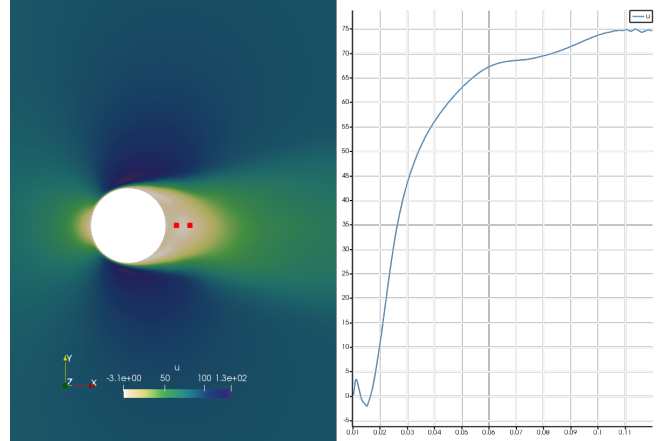


Figure 19: Time average solution of the axial velocity of a circle at $Re = 3900$.

It appears that the size of the recirculation is underpredicted Kravchenko and Moin (2000). This is certainly due to 2-dimensionality constrains on the turbulence—which is intrinsically 3-dimensional.

7 Increasing the *Reynolds*

By increasing the *Reynolds* number to 3900, the flow is supposed to be turbulent and we should observe vortex shedding. Due to the symmetry plane, there is no cross-flow on the y -axis. Thus, a non-symmetrical case was performed to circumvent this issue. To increase the *Reynolds*, the viscosity was lowered and this leads to a maximal y – plus < 7 . Figure 18 show an averaged axial velocity field which exhibits a recirculation zone. To validate this case, the canonical circle was also computed (see Fig. 19).

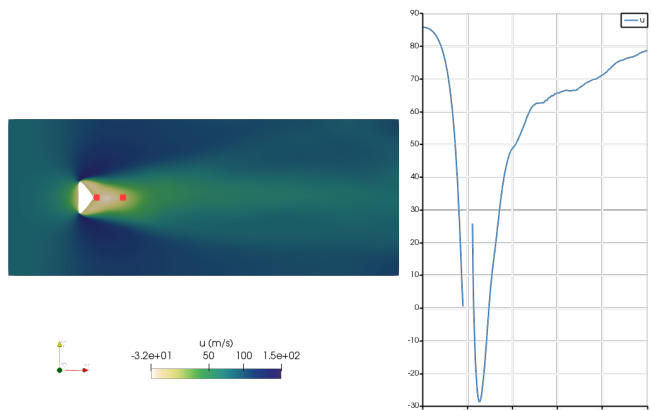


Figure 18: Time average solution of the axial velocity of a bluff body at $Re = 3900$.

8 Perspectives

From these experiments, the goal would be to optimize and measure the uncertainties on the recirculation zone in a bluff body configuration. The DoE would consist in one control point and some modes of a Gaussian perturbation on the shape of the bluff body Degennaro et al. (2015); Roy (2017). The analysis would rely on a surrogate model constructed with *Evofusion*. The high fidelity would consist in a 3-dimensional computation of the case—after a complete validation of the canonical cylinder case—, and the low fidelity would be a 2-dimensional computation. Results from this surrogate would be compared to *Multi-Level Monte-Carlo* results for the mean and variance of the QoI.

Aside from this application, this method will be applied on hydraulique cases. The levels of fidelity would consist in different mesh resolutions.

References

- Marc C Kennedy and Anthony O'Hagan. Predicting the Output from a Complex Computer Code When Fast Approximations Are Available. *Biometrika*, 87(1):1–13, 2000.
- Nicolas Courrier, Pierre Alain Boucard, and Bruno Soulier. Variable-fidelity modeling of structural analysis of assemblies. *Journal of Global Optimization*, 64(3):577–613, 2016. ISSN 15732916. doi: 10.1007/s10898-015-0345-9.
- Alexander I.J. Forrester, Neil W Bressloff, and Andy J Keane. Optimization using surrogate models and partially converged computational fluid dynamics simulations. *Proceedings of the Royal Society A: Mathematical, Physical and Engineering Sciences*, 462(2071):2177 –2204, 2006. ISSN 1364-5021. doi: 10.1098/rspa.2006.1679. URL <http://rspa.royalsocietypublishing.org/content/462/2071/2177.abstract> [{}5Cnhttp://rspa.royalsocietypublishing.org/content/462/2071/2177].
- Alexander I.J. Forrester, András Sóbester, and Andy J Keane. Multi-fidelity optimization via surrogate modelling. *Proceedings of the Royal Society A: Mathematical, Physical and Engineering Sciences*, 463(2088):3251–3269, dec 2007. ISSN 1364-5021. doi: 10.1098/rspa.2007.1900. URL <http://www.jstor.org/stable/20209374> [{}5Cnhttp://rspa.royalsocietypublishing.org/cgi/doi/10.1098/rspa.2007.1900].
- Amandine Marrel, Bertrand Iooss, Béatrice Laurent, and Olivier Roustant. Calculations of Sobol indices for the Gaussian process metamodel. *Reliability Engineering and System Safety*, 94(3):742–751, 2009. ISSN 09518320. doi: 10.1016/j.ress.2008.07.008.
- Bertrand Clarke, Ernest Fokoue, and Hao Helen Zhang. *Breakthroughs in Statistics 2*. Springer Series in Statistics. Springer New York, New York, NY, 1992. ISBN 978-0-387-94039-7. doi: 10.1007/978-1-4612-4380-9. URL <http://link.springer.com/10.1007/978-0-387-98135-2> [{}5Cnhttp://link.springer.com/10.1007/978-1-4612-4380-9].
- Arthur G. Kravchenko and Parviz Moin. Numerical studies of flow over a circular cylinder at ReD=3900. *Physics of Fluids*, 12(2):403–417, 2000. ISSN 10706631. doi: 10.1063/1.870318.
- Philippe Parnaudeau, Johan Carlier, Dominique Heitz, and Eric Lamballais. Experimental and numerical studies of the flow over a circular cylinder at Reynolds number 3900. *Physics of Fluids*, 20(8), 2008. ISSN 10706631. doi: 10.1063/1.2957018.
- A. M. Degennaro, C. W. Rowley, and L. Martinelli. Uncertainty Quantification for Airfoil Icing. *arXiv preprint*, pages 1–16, 2015. doi: 10.2514/1.C032698.
- Pamphile Tupui Roy. Uncertainty Quantification-driven Robust Optimization of a Swirler's Geometry. In *INCA*, page 7, 2017.